The $M_{BH}-M_*$ relation for X-ray-obscured, red QSOs at $1.2 < z < 2.6$

A. Bongiorno,[1]★ R. Maiolino,[2,3] M. Brusa,[4,5,6] A. Marconi,[7] E. Piconcelli,[1]
A. Lamastra,[1] M. Cano-Díaz,[1,8] A. Schulze,[9,10] B. Magnelli,[11] C. Vignali,[4] F. Fiore,[1]
N. Menci,[1] G. Cresci,[12] F. La Franca[13] and A. Merloni[6]

[1]*INAF - Osservatorio Astronomico di Roma, Via di Frascati 33, I-00040 Monteporzio Catone, Rome, Italy*
[2]*Cavendish Laboratory, University of Cambridge, 19 J. J. Thomson Ave, Cambridge CB3 0HE, UK*
[3]*Kavli Institute for Cosmology, Madingley Road, Cambridge CB3 0HA, UK*
[4]*Dipartimento di Astronomia, Università di Bologna, Via Ranzani 1, I-40127 Bologna, Italy*
[5]*INAF - Osservatorio Astronomico di Bologna, via Ranzani 1, I-40127 Bologna, Italy*
[6]*Max Planck Institut für Extraterrestrische Physik, D-85478 Garching, Germany*
[7]*Dipartimento di Astronomia e Scienza dello Spazio, Università degli Studi di Firenze, Largo E. Fermi 2, I-50125 Firenze, Italy*
[8]*Instituto de Astronomía, Universidad Nacional Autonóma de México, A.P. 70-264, 04510 D.F, Mexico*
[9]*Kavli Institute for the Physics and Mathematics of the Universe (Kavli IPMU, WPI), Todai Institutes for Advanced Study, the University of Tokyo, Kashiwa 277-8583, Japan*
[10]*Kavli Institute for Astronomy and Astrophysics, Peking University, 100871 Beijing, China*
[11]*Argelander-Institut für Astronomie, Universität Bonn, Auf dem Hügel 71, D-53121 Bonn, Germany*
[12]*INAF - Osservatorio Astrofisico di Arcetri, Largo E. Fermi 5, I-50125 Firenze, Italy*
[13]*Dipartimento di Matematica e Fisica, Universitaà degli Studi 'Roma Tre', Via della Vasca Navale 84, I-00146 Roma, Italy*

ABSTRACT

We present near-infrared (NIR) spectra, obtained with SINFONI and XShooter observations at ESO VLT, of nine dusty, red QSOs at $1.2 < z < 2.6$. The sources are hard X-ray detected, characterized by cold absorption ($N_H > 10^{21}$–10^{22} cm^{-2}) and show a broad Hα component in the NIR spectra. We complement this sample with 12 additional sources taken from the literature with similar properties resulting in a total sample of 21 X-ray-obscured, intermediate-type (1.8–1.9), dusty reddened QSOs. From the broad Hα line, we have computed the black hole (BH) masses through the virial formula and derived Eddington ratios. Moreover, from optical/IR multicomponent spectral energy distribution fitting we have derived the stellar mass of their host galaxies and their star formation rates. We find that most of the sources in our sample are hosted in starburst and main-sequence star-forming galaxies with Eddington ratios $\lambda > 0.1$. We find a strong trend with the BH mass, i.e. less massive objects are scattered below and above the local relation while the most massive ones are mainly located above it. We also studied the evolution of these sources on the $M_{BH}-M_*$ plane compared to a sample of optically blue type-1 QSOs and we find that obscured red QSOs show a ratio of M_{BH} to M_* that increases with redshift which is consistent with or slightly lower than what has been found for blue QSOs. These sources may represent the blow-out phase at the end of the rapid BH growth and immediately preceding the classical blue QSOs typically sampled in optical surveys. They in fact show evidence of outflows in the ionized gas component, but their BH has already fully formed.

Key words: galaxies: active – galaxies: evolution – quasars: emission lines – quasars: supermassive black holes – cosmology: observations.

1 INTRODUCTION

Tight scaling relations between the central black hole (BH) mass and various properties of their host galaxies in the local Universe (velocity dispersion of the bulge component, σ, stellar masses, M_*, luminosity), have been discovered after the launch of the *Hubble*

★ E-mail: angela.bongiorno@oa-roma.inaf.it

Space Telescope nearly 20 years ago. These correlations (Magorrian et al. 1998; Ferrarese & Merritt 2000; Marconi & Hunt 2003; Häring & Rix 2004) have revolutionized the way we conceive the physical link between galaxy and AGN evolution, suggesting a possible physical coupling between BHs and host galaxies in their evolution.

The local scaling relations, although important in establishing the role of supermassive black holes (SMBHs) in galaxy evolution, have been unable to uniquely determine the physical nature of the SMBH–galaxy coupling. A large number of theoretical models (some including feedback) have been proposed which can reproduce them reasonably well (Silk & Rees 1998; Granato et al. 2004; King 2005), but make different predictions for their redshift evolution. Constraining the high-z $M_{BH}-M_*$ plane is thus of fundamental importance in discriminating between different models but it is unfortunately observationally complex. First of all, we have to rely on less-accurate, single-epoch virial mass estimators based on broad AGN emission lines. Moreover, in deriving the host galaxy properties, we are limited by the presence of the bright nucleus.

At high redshift, most studies of the $M_{BH}-M_*$ relationship have focused on optically blue type-1 broad-line AGN (e.g. Peng et al. 2006; Maiolino et al. 2007b; Jahnke et al. 2009; Decarli et al. 2010; Merloni et al. 2010; Salviander & Shields 2013; Schramm & Silverman 2013) for which the UV broad lines (e.g. Mg II and C IV, observed in the optical band at high-z) are detected and virial formulas can be used to derive BH masses from the AGN luminosity and the width of the broad lines (see e.g. Peterson 2013; Shen 2013, for recent reviews). The emerging picture (see Kormendy & Ho 2013, for a comprehensive picture) points towards a mild or absent evolution of the average BH-to-host-galaxy-mass ratio up to $z \sim 1$ (Jahnke et al. 2009; Cisternas et al. 2011; Schramm & Silverman 2013) and a positive one for $z > 1$ (e.g. Decarli et al. 2010; Merloni et al. 2010; Bennert et al. 2011). In particular, putting together all available observations of AGN at $z \sim 0.1$–7.1 that have reliable estimates of M_{BH}, of the stellar masses of the host galaxies, and of bulge-to-disc ratios (for low-z objects only), Kormendy & Ho (2013) find that the $M_{BH}/M_{*,\text{bulge}}$ evolves as $(1 + z)^\beta$, with $\beta = 0.7$–2. The above results, have been interpreted either as evidence that BHs form faster, at earlier epochs, than their host galaxies, or as due to an evolution of the intrinsic scatter of the $M_{BH}-M_*$ relation (or a combination of both effects). However, the sign of evolution seems to weaken at $z < 2$ when considering the total galaxy mass for galaxies that are not bulge dominated (Jahnke et al. 2009; Kormendy & Ho 2013).

According to theoretical models (e.g. Hopkins et al. 2006; Menci et al. 2006; Lamastra et al. 2010), the positive evolution found for unobscured bright AGN at high redshift, can be interpreted as the fact that galaxy mergers, the driving mechanism for feeding BHs in bright QSOs, are more common at higher redshift, and are thus able to increase the BH accretion rate more rapidly than the star formation rate (SFR) at such redshifts. In contrast, at lower redshift ($z < 1$), for moderate-luminous, Seyfert-like objects with lower BH masses living in spiral-galaxy, secular galaxy evolution, occurring mostly in galaxy discs, would increase the stellar masses, with BH accretion proceeding at a lower rate. A radical alternative for explaining the $M_{BH}-M_{\text{bulge}}$ relation emerges from the statistics of mass averaging in galaxy mergers. This idea, first proposed by Peng (2007), has been elaborated using more realistic semi-analytic models of galaxy formation properly embedded in Λ cold dark matter merger trees by Jahnke & Macciò (2011). According to these simulations, the creation of the scaling relations can be fully explained by the hierarchical assembly of BH and stellar mass

through galaxy merging, from an initially uncorrelated distribution of BH and stellar masses in the early universe.

In contrast to the observational results mentioned above, Alexander et al. (2008) found that for AGN hosted in submm selected galaxies (SMGs) at $2 < z < 2.6$, the growth of SMBHs actually lags that of the host stellar mass. The apparently contradictory behaviour can be interpreted as a selection bias possibly affecting in the opposite way these studies. In fact, studying luminous AGN we are biased towards selecting the most massive SMBHs (see Lauer et al. 2007; Merloni et al. 2010; Schulze & Wisotzki 2011), while a sample of SMGs will be biased towards massive stellar hosts (see Lamastra et al. 2010) since the galaxies that are undergoing the most intense star formation (SF) at $z \sim 2$ also appear to be massive galaxies at this epoch (e.g. Papovich et al. 2006). In addition to possible bias in the sample selection, quasars with different properties may represent different phases in BH and galaxy evolution.

Although SMGs are very interesting high-z ($\sim$2; e.g. Chapman et al. 2005) objects with large SF activities (up to few 1000 $M_\odot$ yr^{-1}; Magnelli et al. 2012), they represent the most extreme class of sources of the entire star-forming galaxy population. New important constraints in understanding the physical nature of the AGN–galaxy coupling require the extension of the analysis of the BH–galaxy relation to the population of X-ray-obscured, dust-reddened QSOs. Current AGN–galaxy co-evolution models predict an early dust-enshrouded phase associated with rapid BH growth triggered by galaxy mergers (Silk & Rees 1998; Di Matteo, Springel & Hernquist 2005; Hopkins et al. 2008). Tidal interactions trigger both violent SF and funnelling of large amount of gas into the nuclear region which feed and obscure the accreting SMBH (e.g. Urrutia, Lacy & Becker 2008; Schawinski et al. 2010). During this phase, we expect the central source to be buried by the surrounding material and the AGN to likely appear as an optically type-2 AGN, X-ray obscured and red (e.g. Hopkins et al. 2008; Menci et al. 2008).

So far, studies on this population are restricted to very few peculiar objects and the statistic is therefore not enough to draw a global picture. The observation of red QSOs is in fact more challenging compared to the blue ones. Measurements of BH masses for red QSOs at $z > 1$ cannot be derived from optical spectroscopy: the UV broad emission lines, used to estimate the BH masses through virial estimators, are not detected due to dust extinction. For these sources, we can detect the AGN optical broad lines, e.g. Hα, redshifted in the NIR, since dust extinction is reduced with respect to the rest-frame UV lines (see Maiolino et al. 2006).

Until recently, there have been only a handful of published works on the evolution of the scaling relations between BHs and host masses for red QSOs: the above-mentioned work of Alexander et al. (2008) based on a sample of four QSOs detected in SMGs, the work from Sarria et al. (2010) based on three hard X-ray-selected, obscured, red QSOs with broad Hα emission line and the most recent work from Urrutia et al. (2012) based on a 2MASS+FIRST selected sample of 13 red QSOs at $0.4 < z < 1$. Sarria et al. (2010) found that the M_{BH}/M_* ratio at $z = 1$–2 is in agreement with the local BH–galaxy relation, and lower than the average M_{BH}/M_* ratio observed in blue QSOs in the same redshift range. However, this result is still tentative since it is based on only three AGN. On the contrary, Urrutia et al. (2012) found that most of the sources in their sample lie below the local relation and that objects below the local relation are the one accreting at high-Eddington ratio ($\lambda = \frac{L_{\text{bol}}}{L_{\text{edd}}} > 0.3$).

Here, we present new IR spectra obtained with SINFONI and XShooter at VLT of nine X-ray-obscured, red QSOs for which a broad Hα component has been observed in the IR spectra. We

complement these data with additional sources available in the literature reaching a final total sample of 21 X-ray-obscured, intermediate-type (Osterbrock 1981), red QSOs with broad Hα emission observed in the near-infrared (NIR). This represents the most extensive study so far for this class of targets. The aim of the paper is to study the $M_{\mathrm{BH}}-M_*$ scaling relation and its evolution for this class of sources by comparing them with the results obtained for optically blue QSOs.

The paper is organized as follows: in Section 2, we will introduce our sample, starting from the new observations and proceeding with the samples taken from the literature and included in our analysis. In Sections 3 and 4, we derive virial BH masses and host galaxy stellar masses. SFRs and Eddington ratios are presented in Section 5. Results on the $M_{\mathrm{BH}}-M_*$ plane are shown in Section 6 followed by the comparison with the semi-analytical model prediction in section 7. Finally, discussion and conclusions are presented in Section 8. Unless otherwise stated, uncertainties are quoted at the 68 per cent (1σ) confidence level.

2 THE SAMPLE

This work is based on new NIR observations (programme 88.B-0316(A) with SINFONI and 090.A-0830(A) with XShooter at the ESO VLT) of hard X-ray-detected, obscured ($N_{\mathrm{H}} \geq 10^{21}$–$10^{22}\,\mathrm{cm^{-2}}$) AGN with red ($R - K \gtrsim 4.5$) colours which show a broad Hα line, integrated with data collected from the literature. The final sample consists of 21 objects, 9 of them are new targets while the remaining 12 are data taken from the literature as listed below. The sample is summarized in Table 1.

2.1 New observations

Our observations were performed with SINFONI and X-Shooter at VLT.

SINFONI observations. We obtained NIR spectra using SINFONI at VLT of 11 hard X-ray selected obscured ($N_{\mathrm{H}} > 10^{22}\,\mathrm{cm^{-2}}$) red ($R - K > 4$) QSOs at $0.7 < z < 2.6$, selected from the *Chandra Deep Field South* (CDFS) (1 Ms exposure; Giacconi et al. 2002). The sources were already spectroscopically classified as type-2 AGN in the optical band and had unambiguous spectroscopic redshifts (GOODS-S; Szokoly et al. 2004). As our sample consisted of sources at different redshifts, observations were obtained in the *J*, *H* and *K* bands to detect the Hα line. The resolutions in the three bands are, respectively, $R = 2000$, $R = 3000$ and $R = 4000$. The requested on-source integration time was 2.3 h. However, of the 11 sources targeted, only 7 have been observed completely while 2 of them were observed for only 1.5 h and the last 2 for 45 min. The typical seeing conditions during the observations were 0.5 –1.1 arcsec.

Data have been reduced by using the ESO-SINFONI pipeline. This pipeline performs the background subtraction, flat-fielding, the spectral calibration of each individual slice, and then reconstructs the cube. Out of these targets we detected a broad Hα component for four of them (three of which are observed for the whole requested time while CDFS633 only for 45 min). Here, we focus on these sources for which the Hα broad component allowed us to infer their BH masses. If we restrict the sample to $z > 1$ and $f_{\mathrm{[2-10\,keV]}} > 1 \times 10^{-15}\,\mathrm{erg\,cm^{-2}\,s^{-1}}$, we have seven objects, four of which with broad H$_\alpha$ detected. At the time of the observations, one source had a wrong redshift estimate and thus the Hα line could not be detected while, for another one, the source was not at the centre of the observed field. Therefore, we can conclude that out of five hard X-ray selected with $f_{\mathrm{[2-10\,keV]}} > 1 \times 10^{-15}\,\mathrm{erg\,cm^{-2}\,s^{-1}}$, obscured

Table 1. Analyzed sample.

ID	RA	Dec.	z
New SINFONI@VLT observations of CDFS AGN			
CDFSX57[a]	03:32:12.9	−27:52:36.9	2.561
CDFSX153[a]	03:32:18.3	−27:50:55.3	1.536
CDFSX531[a]	03:32:14.4	−27:51:10.9	1.544
CDFSX633[a]	03:31:50.4	−27:52:12.2	1.374
New XShooter@VLT observations of COSMOS AGN			
COSMOS18[b]	10:00:31.9	+02:18:11.8	1.606
COSMOS60053[b]	10:01:09.2	+02:22:54.7	1.582
COSMOS175[b]	09:58:53.0	+02:20:56.4	1.530
COSMOS2028[b]	10:02:11.3	+01:37:06.6	1.592
COSMOS5321[b]	10:03:08.8	+02:09:03.5	1.470
Re-analysis of the Sarria et al. (2010) data			
XMMES1_460[c]	00:36:41.5	−43:20:38.1	1.748
Ab2690_29 [d]	00:01:11.4	−25:12:05.1	2.087
BPM1627_181[d]	00:50:31.6	−52:06:30.0	1.335
Alexander et al. (2008)			
A1236+6214	12:36:35.5	+62:14:24.0	2.015
A1237+6203	12:37:16.0	+62:03:23.0	2.053
A1312+4239	13:12:15.2	+42:39:00.0	2.555
A1312+4238	13:12:22.3	+42:38:14.0	2.560
A1636+4059	16:36:55.8	+40:59:14.0	2.592
A1637+4053	16:37:06.5	+40:53:13.0	2.375
Melbourne et al. (2011)			
DOG2	14:33:35.6	+35:42:43.0	1.300
DOG3	14:34:00.3	+33:57:14.0	1.684
Del Moro et al. (2009)			
2XMMJ1232+2152	12:32:04.91	+21:52:55.4	1.870

[a]IDs from Giacconi et al. (2002); [b]IDs from Cappelluti et al. (2009);
[c]ID from Feruglio et al. (2008); [d]IDs from Mignoli et al. (2004).

($N_{\mathrm{H}} > 10^{22}\,\mathrm{cm^{-2}}$) red ($R - K > 4$) QSOs at $1.0 < z < 2.6$, we detect a broad H$_\alpha$ line in 4/5 of the sample.

XShooter observations: NIR spectra have been obtained using XShooter at VLT (Vernet et al. 2011) of 10 X-ray-obscured and -luminous AGN at $1.25 < z < 1.72$ selected from the COSMOS field (i.e. *XMM*-COSMOS sample; Hasinger et al. 2007; Cappelluti et al. 2009; Brusa et al. 2010). The parent sample consisted of ~150 'obscured QSOs' candidates, selected on the basis of their red optical colours ($R - K > 4.5$) and high X-ray-to-optical flux ratio and/or bright IR emission compared to the optical one (see Brusa et al. 2010, section 7 for details). Among them, the observed sample consisted of the six *K*-brightest sources in the $1.25 < z < 1.72$ redshift range with only photometric redshift available, plus four spectroscopically confirmed objects satisfying the same redshift and magnitude selection (three narrow-line objects and one broad-line AGN). Compared to the CDFS sources, these sources are brighter thus extending the range of luminosities covered by our sample to higher values. The exposure times ranged from 1 to 2 h with typical seeing conditions of 0.5 –1.0 arcsec. Spectra have been taken with a resolution of $R = 5100$ (0.9 arcsec slit). The reduction has been done using REFLEX 2.4. A detailed description of the full sample, data reduction and analysis can be found in Brusa et al. (2014). Here, we focus on five sources at $L_{\mathrm{X}} \sim 10^{44}\,\mathrm{erg\,s^{-1}}$ and $N_{\mathrm{H}} > 10^{21-22}\,\mathrm{cm^{-2}}$

for which a broad Hα component has been detected and hence BH masses could be computed. One of these sources is COSMOS2028, whose VLT/SINFONI spectra have been already published by Banerji et al. (2012, ULASJ1002+0137). Given the lower resolution of their spectra ($R = 1500$), Banerji et al. (2012) could not deblend the narrow and broad Hα components. The measured full width at half-maximum (FWHM) and consequently the BH mass is thus lower than the one obtained in this work. If we consider the $z > 1$ and $f_{[2-10\,\mathrm{keV}]} > 1 \times 10^{-14}\,\mathrm{erg\,cm}^{-2}\,\mathrm{s}^{-1}$ sources, we find that 5/6 of the observed sources have Hα broad detected.

From these two observational campaigns, we thus find that, selecting hard X-ray obscured AGN with red colours, we are able to build a highly complete sample of objects ($\geq$80 per cent) with broad Hα emission lines, above a certain flux.

Overall, we have obtained a final sample of nine sources with broad Hα component. We fitted the line profile as explained in Section 3.1 and derived the FWHM of the line. Stellar masses have been computed with a two-component spectral energy distribution (SED) fitting procedure as explained in Section 4.

2.2 Additional sources

In order to increase the statistic of the study, we complemented the new data with a collection of high-z sources taken from the literature with similar properties. Following is the list of included samples.

(i) *Three QSOs from Sarria et al. (2010)*
We include in our sample three X-ray-obscured, red ($R - K > 5$) QSOs from Sarria et al. (2010). IR spectra of hard X-ray sources detected in the Hellas2XMM (Fiore et al. 2003) and ELAIS-S1 survey (Feruglio et al. 2008) have been taken with SINFONI and Isaac, and a broad Hα line has been detected in three cases. This sample is the most similar to our new observations. For these objects, we re-analysed the spectra after improving the reduction, sky subtraction and extraction.

(ii) *Six QSOs hosted in SMGs from Alexander et al. (2008)*
We include in our work a sample of six SMGs that host X-ray-identified obscured AGN with broad Hα line from Alexander et al. (2008). Four of these sources (the ones with available stellar masses measured from Hainline et al. 2011) were already reported in Sarria et al. (2010). Here, we recomputed the stellar masses for all of the six sources using the SED fitting method as explained in Section 4 after collecting the available photometry from the literature. BH masses have been recomputed using the Hα FWHM measurements reported in Alexander et al. (2008) but differently from them, we used the de-absorbed X-ray luminosity (Mushotzky et al. 2000; Alexander et al. 2003; Manners et al. 2003) instead of the continuum 5100Å luminosity (see discussion in Section 3). The latter can in fact be absorbed and/or dominated by the stellar continuum.

(iii) *Two QSOs hosted in ULIRGs from Melbourne et al. (2011)*
We include in our sample two X-ray-obscured AGN hosted in ultra luminous red galaxies (ULIRGs) observed with the Keck laser guide star adaptive optics system and the OSIRIS Integral Field Spectrograph from Melbourne et al. (2011). The targets (four in total) were selected from optical and mid-infrared (MIR) colours of the NOAO Deep Wide-Field Survey of Boötes to be dust obscured galaxies (DOGs; Dey et al. 2008) and to have strong Hα emission. BH masses have been recomputed using the formula derived in Section 3 and since only two sources are detected in the 5 ks *Chandra* X-ray observations of the Boötes field (Kenter et al. 2005), we include only these two in our analysis. As already pointed out by Melbourne et al. (2011), the use of X-ray luminosity leads

to larger BH mass estimates, as expected by the fact that the rest-frame optical continuum is likely absorbed by dust. Stellar masses have been recomputed using the SED fitting technique as explained in Section 4, after collecting the available photometry from the literature.

(iv) *A QSO from Del Moro et al. (2009)*
We include in our sample also a QSO at $z = 1.87$ from Del Moro et al. (2009). This object has been selected as the most extreme X-ray-to-optical flux ratio (EXOs) sources amongst the sample of bright X-ray selected EXOs obtained by cross-correlating XMM-Newton serendipitous source catalogue (2XMMp) and Sloan Digital Sky Survey 9 (SDSS) catalogue. New United Kingdom Infrared Telescope optical/NIR photometry and Multi-Object Infrared Camera and Spectrograph for the Subaru Telescope (MOIRCS) IR spectroscopy have been presented in Del Moro et al. (2009). X-ray luminosity and FWHM of the broad Hα line, available in Del Moro et al. (2009), have been used to compute the BH masses using the formula derived in Section 3 while stellar masses have been derived from the K-band absolute magnitude. Del Moro et al. (2009) measure a K-band apparent magnitude of 19.9 in AB system, that converted in the K-band absolute magnitude corresponds to $M_k = -25.74$. Assuming the relations between M_* and L_k for star-forming and quiescent galaxies found by Ilbert et al. (2010), we estimated $\log M_* = 12.23 \pm 0.2$.[1]

2.3 Comparison sample of optical type-1 blue QSOs from Merloni et al. (2010)

As a comparison sample, we used a sample of ∼90 unobscured, optically type-1, blue QSOs ($R - K \sim 2$–3, Brusa et al. 2007) from the zCOSMOS survey in the redshift range $1 < z < 2.2$, presented in Merloni et al. (2010). For consistency with our X-ray selection, only sources with *XMM* detections (82/89) have been included in the analysis. Merloni et al. (2010) computed their BH masses using the virial formula from McGill et al. (2008). However, since we want to use these objects as comparison sample of the obscured one, we recomputed the BH masses using the Mg II line and the 3000 Å continuum luminosity as described in Section 3, by adopting the same calibration method as for the obscured sample (equation 3). For blue, unobscured QSOs, the continuum L_{3000} is not expected to be severely affected by obscuration and can therefore be used in the virial equation. For the stellar masses, since the method used by Merloni et al. (2010) is the same used in this paper, we do not recompute them but we use the ones provided in their table 1.

3 BH MASS ESTIMATES

BH masses have been obtained using the relation which combines the virial theorem with the radius–luminosity relation and provides mass estimates which are dubbed as 'single epoch', in contrast to the mass estimates from reverberation mapping observations (e.g. Peterson et al. 2004; Vestergaard & Peterson 2006). The relation for single-epoch mass estimates can be written as

$$\log M_{\mathrm{BH}} = \alpha + 2 \log v_{1000} + \beta \log L_{44}, \tag{1}$$

where L_{44} is the luminosity estimator in units of 10^{44} erg s^{-1} and v_{1000} is the velocity estimator in units of 1000 km s^{-1}. β is the slope of the radius–luminosity relation which connects the size of the

---

[1] we note here that the average M_*/L_k ratio of the sources of our sample for which the SED fitting procedure has been applied, fit well with this relation.

broad-line region (BLR) with the continuum luminosity (e.g. Kaspi et al. 2000; Bentz et al. 2009). The normalization α is calibrated by assuming that the single epoch masses are in agreement with reverberation mapping masses (Vestergaard & Peterson 2006) which, in turn, are in agreement with the $M_{BH}-\sigma$ relation for normal galaxies (Onken et al. 2004). Such approach is motivated by the unknown geometry and kinematics of the BLR (see e.g. McLure & Dunlop 2001; Onken et al. 2004). However, due to the different choices adopted in the calibration, a large number of different relations are reported in the literature that relate BH mass, broad-line width and continuum luminosity (e.g. McGill et al. 2008; Kormendy & Ho 2013). The key point for this paper is that the BH–galaxy scaling relation adopted to calibrate β should be the same or be consistent with the scaling relation at $z = 0$ used as a reference for studying the redshift evolution.

Here, we adopt a relation which has been calibrated by directly imposing that single-epoch masses agree with the local BH–galaxy scaling relations (Marconi et al., in preparation). Briefly, single-epoch virial products (i.e. BH masses for $\alpha = 0$) have been estimated from Hβ using the average spectra for the objects of the reverberation mapping data base by Peterson et al. (2004) updated with the measurements from the most recent campaigns. In the case of Mg II, we have used the spectral measurements from International Ultraviolet Explorer data performed by Wang et al. (2009). BH masses have been estimated from the stellar velocity dispersion (see e.g. Park et al. 2012, for a compilation of data), or from the luminosity (Bentz et al. 2009) of the host spheroid using the $M_{BH}-\sigma$ and/or $M_{BH}-L_V$ relations by Gültekin et al. (2009). The adopted relations can be expressed in the form

$$\log M_{BH} = 6.7 + 2 \log \left(\frac{\text{FWHM}_{H\beta}}{10^3 \text{ km s}^{-1}} \right) + 0.5 \log \left(\frac{\lambda L_\lambda(5100 \text{ Å})}{10^{44} \text{ erg s}^{-1}} \right) \tag{2}$$

$$\log M_{BH} = 6.6 + 2 \log \left(\frac{\text{FWHM}_{Mg II}}{10^3 \text{ km s}^{-1}} \right) + 0.5 \log \left(\frac{\lambda L_\lambda(3000 \text{ Å})}{10^{44} \text{ erg s}^{-1}} \right), \tag{3}$$

where FWHM refers to the Hβ and Mg II broad lines and L_λ(5100 Å) and L_λ(3000) represent the AGN continuum luminosity λL_λ at 5100 and 3000 Å, respectively. Uncertainties on the normalization, i.e. α, are of the order of 0.1 dex (see Marconi et al., in preparation for more details). In the following, for the comparison with the $z = 0$ relation, we will use as a reference the $M_{BH}-M_\star$ relation by Sani et al. (2011) because the sample adopted by those authors defines an $M_{BH}-\sigma$ relation consistent with that of Gültekin et al. (2009).

To compute the BH masses of the objects in our sample, we used equation (2) after converting Hβ in Hα using the correlation between Hα and Hβ widths found by Greene & Ho (2005). Moreover, since our sample is made of dust-reddened QSOs, the continuum luminosity at 5100 Å is expected to be absorbed and/or strongly contaminated by stellar continuum. For this reason, we replaced λL_λ(5100 Å) with the absorption corrected X-ray [2−10] keV luminosity using equation 5 of Maiolino et al. (2007a). We obtain for the BH mass the following expression:

$$\log M_{BH} = 7.11 + 2.06 \log \frac{\text{FWHM}_{H\alpha}}{10^3 \text{ km s}^{-1}} + 0.693 \log \frac{L_{[2-10 \text{ keV}]}}{10^{44} \text{ erg s}^{-1}}. \tag{4}$$

For our statistical analysis of the scaling relation evolution, we assign to each BH mass measurement an error given by the sum of the statistical and systematic uncertainties. The systematic uncertainty in the $\log M_{BH}$ determination has been estimated in 0.3 dex to account for the observed scatter in the virial relation itself, while in the computation of the statistical errors, we take into account the errors in the X-ray luminosity[2] and FWHM measurements, together with the uncertainties associated with the $L_{[2-10 \text{ keV}]}-L_{5100}$ relation coefficient which contributes with 0.07 dex (in quadrature).

3.1 FWHM measurements

We measured the FWHM in the nine new IR spectra presented here plus the three sources taken from Sarria et al. (2010) for which we re-analysed the spectra after improving the sky subtraction and extraction. Following Sarria et al. (2010), the broad Hα component detected in the IR spectra has been fitted with a broad Gaussian and one or more narrow Gaussians accounting for the contribution of the narrow components of both Hα and [N II]. The underlying continuum has been fitted with a linear component. Regions affected by low S/N and/or bad sky residuals are not taken into account in the fit. We linked the narrow components of Hα and [N II] to have the same velocity shift and the same velocity dispersion. Moreover, the flux of the [N II]λ6548 line was linked to be one-third of the [N II]λ6584 line. The uncertainty in the width of the broad line is estimated by accounting for the correlation with the other components. A zoom of the 12 analysed spectra around the region of the broad Hα line, together with the line fit is shown in Fig. 1. For the rest of the sources, we have taken the FWHM published values.

Rest-frame FWHM values are reported in Table 2. As explained above, the measured FWHM of the Hα broad component has been used, together with the de-absorbed X-ray [2−10] keV luminosity in equation (4) to compute the BH masses.

3.2 Intrinsic X-ray luminosity estimates

Intrinsic X-ray [2–10 keV] luminosities have been computed after correcting the flux for the absorption N_H. When possible, N_H values have been derived directly by fitting the X-ray spectra. On the contrary, for sources detected with few counts, for which a proper X-ray spectral analysis cannot be performed, we have used the hardness ratio (computed as HR = $(H − S)/(H + S)$, where S and H are the soft and hard band counts) as a measure of obscuration. For the nine sources for which new observations are presented, we have performed a fit of the X-ray spectra (for details, see Mainieri et al. 2007, 2011; Merloni et al. 2014) for all but COSMOS60053, for which the quality of the X-ray data is low. For these sources, the N_H is typically constrained within 0.1 dex. This translates into uncertainties on the rest-frame X-ray fluxes (and therefore luminosities) from <5 per cent for the brightest sources to ~20 per cent for the faintest ones. For the remaining sources, the N_H values have been taken from literature or derived from the hardness ratio (as specified in Table 2) assuming a power-law X-ray spectrum with a typical photon index $\Gamma = 1.8$ (Piconcelli et al. 2005).

Since X-ray luminosities are used, together with the FWHM, to compute the BH masses, it is important to be sure that the derived values are robust. To this end, we have used the MIR/X-ray luminosity ratios (Fiore et al. 2008; Gandhi et al. 2009; Lanzuisi et al. 2009) to check the consistency of the L_X with the whole SED of the source (see Section 4). We find that the agreement is good for all but six

---

[2] an average 10 per cent error in the X-ray luminosities of all sources has been assumed in computing the BH masses.
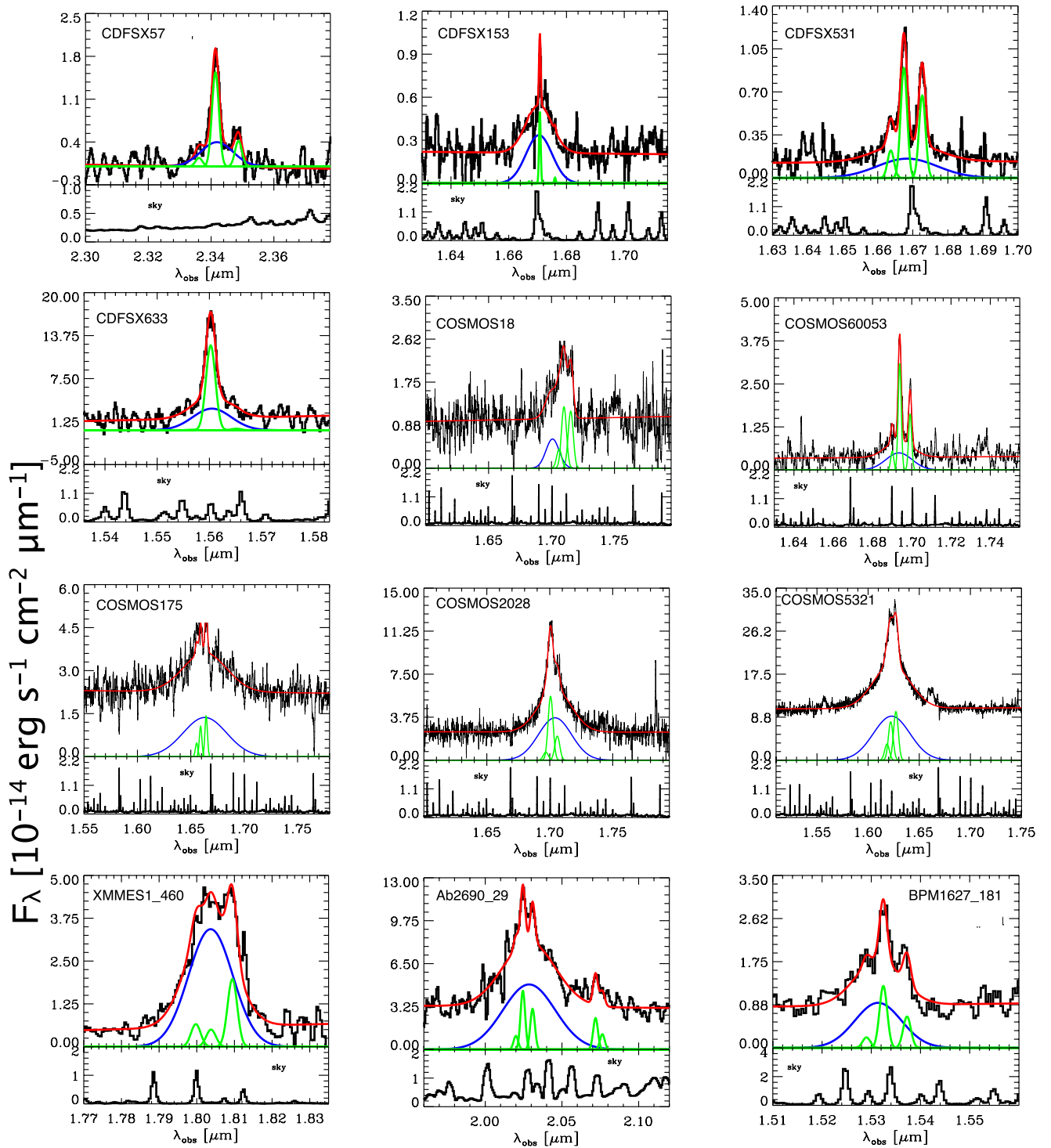
Figure 1. Zoom-in showing the broad Hα line of the NIR spectra of the 9 X-ray-obscured and red QSOs for which a broad Hα component has been observed in XShooter and SINFONI. The last three spectra correspond to the objects already published in Sarria et al. (2010) for which we present the new reduction and fit. The blue line shows the broad Hα Gaussian component while the green one corresponds to the narrow components for Hα and [N II]. Finally, the red line is the resulting fit. The bottom panel of each plot shows the sky spectrum.

sources. In three of these objects, the discrepancy is however relatively small (corresponding to an ∼0.3 dex difference in luminosity) and can be ascribed to the large scatter present in the MIR/X-ray ratio used (Gandhi et al. 2009). In contrast, for the remaining three

objects (CDFSX633, A1236+6214 and A1237+6203), the discrepancy is larger i.e. ∼0.5–0.6 dex in X-ray luminosity. In these cases, there is the possibility that the X-ray luminosity as derived by the X-ray data may not be reliable due to an underestimate of the N_H

Table 2. Physical quantities for the selected sample. Stellar masses are computed using the Chabrier IMF. Objects marked with [(*)] are sources for which we report in the table the new corrected SED-derived L_X (see Section 4). The L_X as measured directly from X-ray data are kept in parenthesis, as well as the BH masses computed using these values. A 10 per cent error is associated with L_X. The reported N_H values are: (a) computed from X-ray spectral analysis; (b) computed from X-ray spectral analysis by Mainieri et al. (2007, 2011); (c) computed from the HR by Merloni et al. (2014); (d) taken from Sarria et al. (2010); (e) computed from the HR in Alexander et al. (2003); (f) computed from the HR in Mushotzky et al. (2000); (g) computed from the HR in Manners et al. (2003); (h) taken from Melbourne et al. (2011); (i) computed from X-ray spectral analysis by Del Moro et al. (2009).

ID	$L^{\rm deabs}_{[2-10\,{\rm keV}]}[{\rm erg\,s^{-1}}]$	$N_{\rm H}[{\rm cm^{-2}}]$	${\rm FWHM_{H\alpha}[Km\,s^{-1}]}$	$\log M_{\rm BH}[{\rm M_\odot}]$	$\log M_*[{\rm M_\odot}]$
CDFSX57	2.3×10^{44}	2.0×10^{23}(a)	1538 ± 498	7.74 ± 0.42	$10.44^{+0.18}_{-0.11}$
CDFSX153	1.1×10^{44}	3.0×10^{23}(a)	1904 ± 185	7.71 ± 0.32	$10.94^{+0.01}_{-0.01}$
CDFSX531	1.1×10^{43}	2.0×10^{23}(a)	3620 ± 714	7.59 ± 0.45	$10.59^{+0.01}_{-0.02}$
CDFSX633[(*)]	7.2×10^{43} [1.5×10^{43}]	[3.0×10^{23}(a)]	1665 ± 557	7.47 ± 0.43 [6.97]	$10.81^{+0.05}_{-0.09}$
COSMOS18	7.5×10^{44}	3.2×10^{22}(b)	2162 ± 531	8.41 ± 0.38	$11.38^{+0.01}_{-0.21}$
COSMOS60053	9.5×10^{43}	$>1.0 \times 10^{20}$(c)	2776 ± 391	8.00 ± 0.33	$11.20^{+0.19}_{-0.41}$
COSMOS175	3.8×10^{44}	2.5×10^{21}(b)	8623 ± 460	9.44 ± 0.31	$11.55^{+0.12}_{-0.21}$
COSMOS2028	1.5×10^{45}	7.9×10^{21}(b)	5423 ± 146	9.44 ± 0.31	$11.91^{+0.05}_{-0.03}$
COSMOS5321	3.8×10^{45}	3.9×10^{21}(b)	7772 ± 87	10.03 ± 0.31	$12.22^{+0.05}_{-0.01}$
XMMES1_460	7.2×10^{44}	3.2×10^{22}(d)	2310 ± 111	8.45 ± 0.31	$10.53^{+0.31}_{-0.38}$
Ab2690_29	8.9×10^{44}	6.3×10^{22}(d)	5871 ± 245	9.35 ± 0.31	$12.00^{+0.03}_{-0.11}$
BPM1627_181	1.6×10^{44}	6.3×10^{22}(d)	2173 ± 330	7.94 ± 0.33	$10.83^{+0.77}_{-0.21}$
A1236+6214[(*)]	3.5×10^{44} [6.3×10^{43}]	[5.0×10^{23}(e)]	1600 ± 200	7.90 ± 0.33 [7.39]	$10.46^{+0.01}_{-0.05}$
A1237+6203[(*)]	5.9×10^{44} [1.2×10^{44}]	3.2×10^{22}(e)	2400 ± 500	8.43 ± 0.36 [7.96]	$10.54^{+0.25}_{-0.11}$
A1312+4239	7.9×10^{44}	1.0×10^{21}(f)	2500 ± 500	8.55 ± 0.35	$11.61^{+0.05}_{-0.23}$
A1312+4238	5.0×10^{44}	1.0×10^{21}(f)	2600 ± 1000	8.45 ± 0.46	$10.59^{+0.06}_{-0.01}$
A1636+4059	1.0×10^{45}	1.0×10^{22}(g)	3000 ± 400	8.79 ± 0.33	$10.92^{+0.12}_{-0.45}$
A1637+4053	$<1.0 \times 10^{44}$	–	3300 ± 1000	<8.18	$11.35^{+0.22}_{-0.39}$
DOG2	2.1×10^{44}	6.1×10^{21}(h)	2288 ± 40	8.07 ± 0.31	$10.47^{+0.41}_{-0.23}$
DOG3	3.9×10^{44}	6.0×10^{20}(h)	6757 ± 96	9.23 ± 0.31	$11.91^{+0.02}_{-0.01}$
2XMMJ1232+2152	1.6×10^{46}	2.0×10^{23}(i)	5280 ± 331	10.12 ± 0.31	$12.23^{+0.20}_{-0.20}$

value caused by the low counts statistics. For these sources, we derived new intrinsic SED-derived X-ray luminosities and we used them in the computation of the BH masses (see the next section). Intrinsic X-ray luminosities are reported in Table 2.

4 GALAXY STELLAR MASS ESTIMATES

Stellar masses of the AGN host galaxies have been derived using a detailed two-component SED fitting procedure (Bongiorno et al. 2012) in which the observed optical-to-NIR SED is fitted with a large grid of models made from a combination of AGN and host-galaxy templates.

For the AGN component, we adopted the Richards et al. (2006) mean QSO SED derived from the study of 259 type-1 quasars with both SDSS and *Spitzer* photometry. We allow for extinction of the nuclear AGN light by applying a SMC-like dust-reddening law (Prevot et al. 1984) of the form: $A_\lambda / E(B-V) = 1.39\lambda_{\mu m}^{-1.2}$. For the galaxy component, we generated a library of synthetic spectra using the models of stellar population synthesis of Bruzual & Charlot (2003). tabWe assumed a universal initial mass function (IMF) from Chabrier (2003), and we built 10 exponentially declining star formation histories (SFHs) SFR $\propto e^{-t_{\rm age}/\tau}$ with *e*-folding times, τ, ranging from 0.1 to 30 Gyr and a model with constant SF. For each of the SFHs, the SED was generated for a grid of 13 ages ranging from 50 Myr to 9 Gyr, subject only to the constraint that the

age should be smaller than the age of the Universe at the redshift of the source. Moreover, dust extinction of the galaxy component has been taken into account using the Calzetti law (Calzetti et al. 2000), which is the most used attenuation curve in high-redshift studies.

This technique, applied to data sets with a wide multiwavelength optical-to-NIR coverage, which is the case for most of our objects, allows us to decompose the entire SED into a nuclear AGN and a host galaxy components and to derive robust measurements of the host galaxy properties, i.e. stellar mass. For more details, we refer the reader to Bongiorno et al. (2012).

In the sample considered here, we used this technique for all but one of the 21 sources. The result of the SED fitting procedure applied to our data is shown in Fig. 2 and the values of the host stellar masses, using a Chabrier IMF, are reported in Table 2. In few cases, the most extreme blue data point shows an excess compared to the whole SED and to the model fit. The excess corresponds to the rest-wavelength of the Lyα emission line and is not taken into account in the fitting procedure. For the remaining source (2XMMJ1232+2152), no multiwavelength photometry was available and hence our estimated stellar mass has been computed from the absolute *K*-band magnitude.

As in the 24 μm flux measures there could be a strong contribution from SF, we also computed the AGN 12 μm fluxes derived from the X-ray luminosities using the Gandhi et al. (2009) relation to
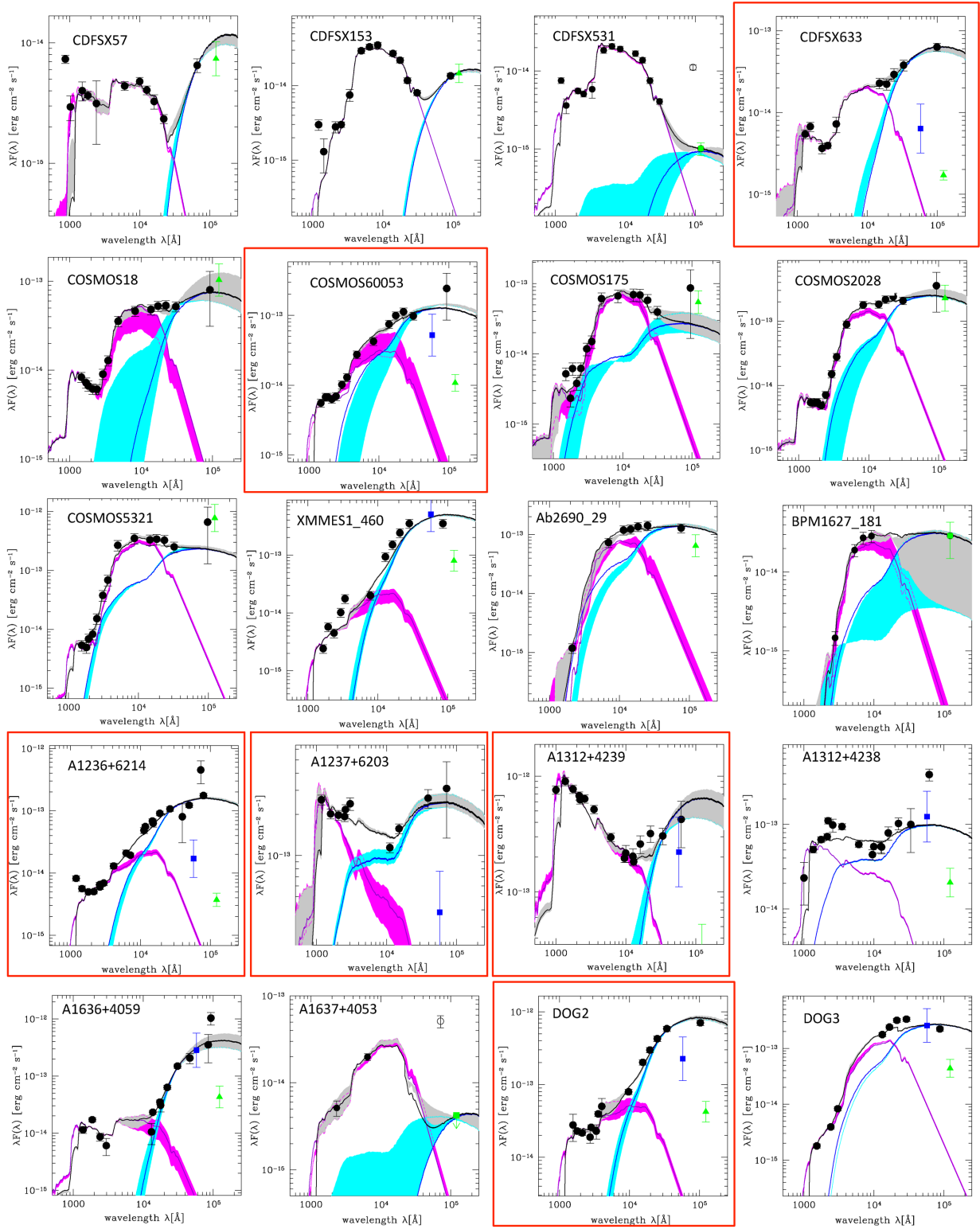
Figure 2. SED fits for the 20 sources for which we derive stellar masses through multiwavelength SED fitting. Black circles are rest-frame fluxes corresponding to the observed bands plotted rest frame. Purple and blue lines correspond to the galaxy and the AGN template found as best-fitting solution through the χ^2 minimization, while the black line shows their sum. Green triangles correspond to the rest-frame 12 μm luminosity predicted from $L_{[2-10 keV]}$ using the relation from Gandhi et al. (2009). This point is taken into account (instead of the 24 μm observed luminosity) in the fit of three sources in which the 24 μm point is absent (BPM1627_181) or clearly contaminated by SF emission (CDFSX531, A1637+4053). In the latter case, the observed 24 μm point is showed as empty circle and the 12 μm one as green square. Blue squares correspond to the 5.8 μm luminosity predicted from $L_{[2-10 keV]}$ using the relation from Lanzuisi et al. (2009). We show this point only for the 10 objects in which the 12 μm luminosity does not seem to agree with the whole SED. Finally, red frames indicate the six cases in which both the rest-frame 12 μm and the 5.8 μm luminosities are in disagreement with the whole SED.

constrain the AGN-only emission. We find that in some cases these two quantities (12 and 24 µm fluxes) are indeed discrepant. In two cases (i.e. CDFSX531, A1637+4053), we have used the AGN 12 µm point derived from the X-ray luminosity to constrain the AGN emission since the whole SED shape was, in terms of χ^2, slightly better constrained. Moreover, for BPM1627_181, no 24 µm observations were available and thus the 12 µm point was used. In these three cases, the observed 24µm point is shown in Fig. 2 as an open circle and indicates that the given stellar mass has been computed anchoring the AGN template to 12µm which is indeed relative only to the nuclear emission.

It is worth noting that, for the source A1637+4053, the scarce observational data points make the fit of this source, and thus M_* poorly constrained. Moreover, the X-ray luminosity of this source is an upper limit and thus it is its M_{BH}.

In other cases (10/20, i.e. CDFSX633, COSMOS60053, XMMES1_460, A1236+6214, A1237+6203, A1312+4239, A1312+4238, A1636+4059, DOG2, DOG3), the 12 µm luminosity derived from the de-absorbed X-ray luminosity is too low to fit the global SED shape. The discrepancy could be ascribed to effects of variability of the X-ray emission between the times of the X-ray and MIR observations. However, a detailed analysis of the light curve of the *XMM*-COSMOS and CDFS samples does not reveal any sign of remarkable variability in their X-ray fluxes (Young et al. 2012; Lanzuisi et al. 2014). However, as already pointed out by Lanzuisi et al. (2009), the relation between X-ray and MIR luminosity found locally by Gandhi et al. (2009) for optically/X-ray bright Seyfert-2 galaxies, does not always fit higher redshift and higher MIR luminosity, red obscured sources (i.e. extreme DOGs, EDOGs defined to have $F_{24\,\mu m}/F_R > 2000$ and $F_{24\,\mu m} > 1.3$mJy). In particular, Lanzuisi et al. (2009, but see also Maiolino et al. 2007b; Fiore et al. 2008) find that X-ray selected QSO2 follow the local relation at all redshifts and luminosities while dust-absorbed powerful (ULIRG-like) nuclei are characterized by extreme MIR/X-ray luminosity ratios. For these sources, a flatter relation is derived (which however shows a large scatter) that, for a given $L_{[2-10\,keV]}$, predicts a higher MIR luminosity compared to the local one. For the sources for which the Gandhi relation does not predict an MIR luminosity in agreement with the whole SED, we thus applied also the Lanzuisi et al. (2009) relation.[3] The new MIR luminosities predicted in this way are shown with blue squares in the SED fit in Fig. 2 of the 10 sources listed above. For four of these cases (XMMES1_460, A1312+4238, A1636+4059 and DOG3), the MIR luminosity predicted by the Lanzuisi relation is in agreement with the one expected by the whole SED. For the remaining six (CDFSX633, COSMOS60053, A1236+6214, A1237+6203, A1312+4239 and DOG2), a discrepancy is still visible. As explained in Section 3.2, for the three sources for which the discrepancy corresponds to a difference of the order of 0.5–0.6 dex in the X-ray luminosity (CDFSX633, A1236+6214 and A1237+6203), we computed new intrinsic X-ray luminosities assuming the MIR luminosity as derived by the SED[4] and applying the relation found by Lanzuisi et al. (2009). These SED-derived L_X of these three sources have been used to compute the BH masses and are reported in Table 2. The original L_X values obtained from

the X-ray data analysis (see Section 3.2) are also listed in Table 2 in parentheses.

5 HOST GALAXY'S SFRs AND BH EDDINGTON RATIOS

In this section, we study and compare the rate at which host galaxies accrete in relation with their BHs. To this end, we have derived the galaxy SFR and BH Eddington ratio for each object in the sample. In general, the most reliable way to compute the galaxy's SFR is adding up the rate of unobscured SF (emitted in the UV) with the obscured one re-emitted in the (mid- and far-) IR by dust (SFR$_{UV + IR}$). However, for bright IR sources, SFR$_{UV}$ is negligible compared to the absorbed one and we can simply assume SFR$_{TOT}$ ∼ SFR$_{IR}$. For this reason, mid- and far-IR measurements of cold dust heated by star-forming processes are in principle the most reliable ways to measure the galaxy's SFR. On the one hand, in the case of bright QSOs, the AGN contamination in the IR band cannot be negligible and thus the derived SFRs slightly overestimated (see e.g. Bongiorno et al. 2012; Mullaney et al. 2012). On the other hand, the optical/IR SED fitting procedure relies only on the UV emission measurements, which traces the unobscured SF and takes into account the obscured component using the dust correction factor computed from the full SED. For the objects in our sample, we estimated the host SFRs using submm/IR data when available and the SED fitting procedure otherwise. The SFR of our sources are inferred from their infrared luminosities using the best set of mid/far-infrared/submm data available. For sources with PACS detections, IR luminosities are derived by fitting their far-infrared flux densities with the SED templates of Dale & Helou (2002). For sources with no far-infrared detection but with a submillimetre detection (i.e. from SCUBA), infrared luminosities are derived from their SCUBA flux densities using the L_{IR}–submm relation of Magnelli et al. (2012). From these IR luminosities, we infer SFRs assuming SFR [$M_\odot$ yr^{-1}] = $10^{-10} \times L_{IR}$ [$L_\odot$] (Kennicutt 1998) for a Chabrier (2003) IMF.

For quantifying the BH accretion, we derived the Eddington ratio, defined as the ratio between the AGN bolometric luminosity and the Eddington luminosity:

$$\lambda_{Edd} = \frac{L_{bol}}{L_{Edd}} = \frac{L_{bol}\,[erg\,s^{-1}]}{1.3 \times 10^{38} \times M_{BH}/M_\odot}, \tag{5}$$

where L_{bol} have been derived from the X-ray luminosities using the bolometric correction derived from Marconi et al. (2004). Galaxy's SFRs and BHs Eddington ratios λ are reported in Table 3.

Fig. 3 shows the starburstiness R_{SB} = sSFR/sSFR$_{MS}$ (sSFR$_{MS}$ being the reference sSFR = SFR/M_* of the galaxies in the main sequence) of the host galaxies versus the BH Eddington ratio. Open circles correspond to the cases for which we have only an upper limit on the SFR while filled circles with an arrow to the objects with log(SFR) < 0. The starburstiness R_{SB} (Elbaz et al. 2011; Lamastra et al. 2013b) measures the excess or deficiency in sSFR of a galaxy in terms of its distance from the galaxy main sequence (sSFR$_{MS}$). For this comparison, we used the best-fit of the galaxy main sequence as a function of redshift obtained by Whitaker et al. (2012).

Following Rodighiero et al. (2011), we define a galaxy to be starburst if its SFR is above four times the main sequence ($R_{SB} > 4$), quiescent if it is below four times the main sequence ($R_{SB} < 1/4$) and main sequence if $1/4 < R_{SB} < 4$ (see also Sargent et al. 2012; Lamastra et al. 2013a). Moreover, we divided the sample in high-accreting BHs ($\lambda > 0.2$) and low-accreting BHs ($\lambda < 0.2$; see Fig. 3).

---

[3] The same result would be obtained using the relation derived by Fiore et al. (2008) since, in the luminosity range spanned by the analysed sample, the two relations are very similar.

[4] Before doing that, we double-checked, with a different SED code which includes the starburst component, that the discrepancy found cannot be ascribed to SF contamination to the 24 µm photometric point.

Table 3. SFRs (Chabrier IMF) in $M_{\odot}$ yr^{-1} and Eddington ratios λ of the analysed sample. *band* indicates which data we used to compute the SFR.

ID	log(SFR)	band	λ
CDFSX57	<2.56	PEP	1.38
CDFSX153	<1.95	PEP	0.56
CDFSX531	1.82 ± 0.07	PEP	0.038
CDFSX633	<1.92	PEP	0.56
COSMOS18	<2.21	PEP	1.31
COSMOS60053	2.87 ± 0.01	PEP	0.24
COSMOS175	<2.14	PEP	0.05
COSMOS2028	2.44 ± 0.01	PEP	0.03
COSMOS5321	2.36 ± 0.01	PEP	0.15
XMMES1_460	$2.41^{+0.14}_{-0.01}$	SED	1.15
Ab2690_29	<0	SED	0.18
BPM1627_181	<0	SED	0.54
A1236+6214	2.73 ± 0.01	PEP	1.66
A1237+6203	2.48 ± 0.19	Scuba	1.0
A1312+4239	2.35 ± 0.14	Scuba	1.00
A1312+4238	2.09 ± 0.18	Scuba	0.75
A1636+4059	3.22 ± 0.12	Scuba	0.74
A1637+4053	3.44 ± 0.16	Scuba	0.16
DOG2	2.56 ± 0.10	SED	0.58
DOG3	2.22 ± 0.10	SED	0.09
2XMMJ1232+2152	−99.0	–	0.46

We find that most (90 per cent) of our sources are hosted in starburst or main-sequence star-forming galaxies with BHs accreting at $\lambda > 0.1$ (80 per cent). No clear trend is visible between BH accretion and host galaxy's SFR. However, we note that starburst galaxies are preferentially found (all but one) to host high-Eddington ($\lambda > 0.2$) AGN.

6 THE $M_{\mathrm{BH}} - M_*$ SCALING RELATION

In Fig. 4, we show the $M_{\mathrm{BH}} - M_*$ plane for our sample which spans the $z \sim 1.2$–2.6 range. As explained in the previous section, for three sources (CDFSX633, A1236+6214 and A1237+6203), the intrinsic X-ray luminosity disagrees with the rest of the SED. These sources are suspected to be highly obscured (possibly Compton thick) AGN for which the measured N_{H} is underestimated due to the poor quality of the X-ray data and therefore the intrinsic luminosity much higher than that derived from the X-ray data. Since the intrinsic X-ray luminosity is used to compute the BH mass, the BH masses associated with these objects could be as well underestimated. For these sources, we thus used the SED-derived L_{X} to derive the BH masses. The values for the BH masses considering the L_{X} obtained from the X-ray data are shown in the plot with the same (but open) symbols as the corresponding subsample.

Since the virial relations used in this work to derive the BH masses are normalized to the Sani et al. (2011) local relation (see Section 3), to study the redshift evolution, high-redshift sources in this plane have to be compared to the above local relation. The Sani et al. (2011) local relation is shown in Fig. 4 with a solid line. From this comparison, we find that, X-ray-obscured, red QSOs are largely scattered around the local scaling relation. In particular, we note that while less massive objects are equally scattered below and above the local relation, the most massive ones are mainly found above. Considering the Eddington ratios of the analysed sources, we find both high- and low-accreting SMBHs equally distributed below and above the local relation. This is in contrast to the work
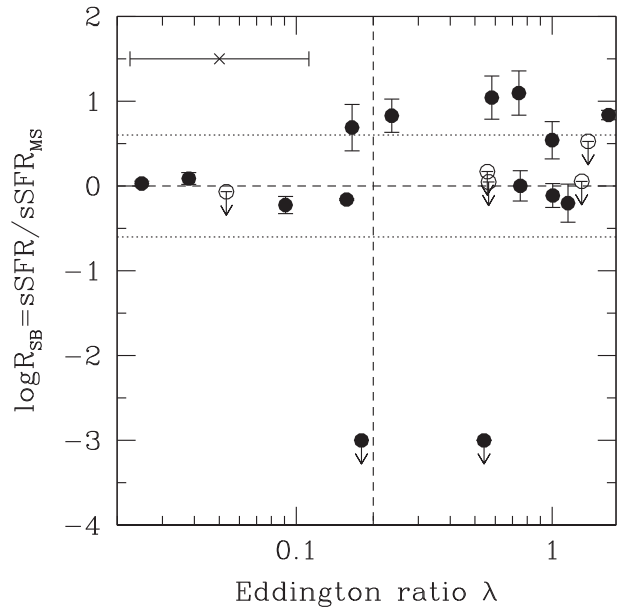
Figure 3. Starburstiness $R_{\mathrm{SB}} = \mathrm{sSFR}/\mathrm{sSFR}_{\mathrm{MS}}$ of the host galaxies versus the BH Eddington ratio. The sSFR values are normalized assuming the best fit of the galaxy main sequence as a function of redshift (horizontal dashed line) obtained by Whitaker et al. (2012). Dotted lines trace four times above and below the main sequence: the three delimited regions are used to define a galaxy to be starburst, main sequence or quiescent (Rodighiero et al. 2011). SFRs have been derived from IR/or submm fluxes when available and from SED-fitting otherwise (see Table 3). Open circles correspond to the cases for which we have only an upper limit on the SFR while filled circle with an arrow correspond to the objects with log(SFR) <0. The cross with the error bar in the upper-left corner shows the average error on the *x*-axis which corresponds to an error of ∼0.35 dex in λ.

from Urrutia et al. (2012), who studied a sample of 13 luminous, red QSOs at $z < 1$, and found that low-accreting SMBHs ($\lambda < 0.3$) lie mainly above the scaling relation while high-accreting SMBHs ($\lambda > 0.3$) below.

Moreover, we note that the position of some sources (i.e. objects taken from Sarria et al. 2010 and Alexander et al. 2008) is different compared to what presented in their original papers. This is due to a more accurate estimate of the stellar masses, a different calibration used to compute the BH masses, the use of the L_{X} instead of the $L_{5100\,\text{Å}}$ in the BH mass formula for the sources in Alexander et al. (2008) and, for BPM1627_181, also to a more accurate FWHM measurement. Differences in the BH mass are below 0.4 dex while the host masses can differ up to 0.7 dex.

6.1 Evolution of the $M_{\mathrm{BH}} - M_*$ scaling relation

In Fig. 5, we plot the offset $\Gamma(z)$ between the M_{BH}/M_* and the local values, calculated as distance in the log space of each point to the Sani et al. (2011) correlation[5] as a function of redshift:

$$\Gamma(z) = \log\left(\frac{M_{\mathrm{BH}}}{M_*}\right)(z) - \log\left(\frac{M_{\mathrm{BH}}}{M_*}\right)(z=0). \quad (6)$$

---

[5] Some of the previous works have defined Γ as the offset from the scaling relations in terms of 'excess BH mass'. To compare this measures with our points we have divided these values by $\sqrt{1 + A^2}$ where A = 0.79 is the slope of the Sani et al. (2011) relation (see also Merloni et al. 2010).
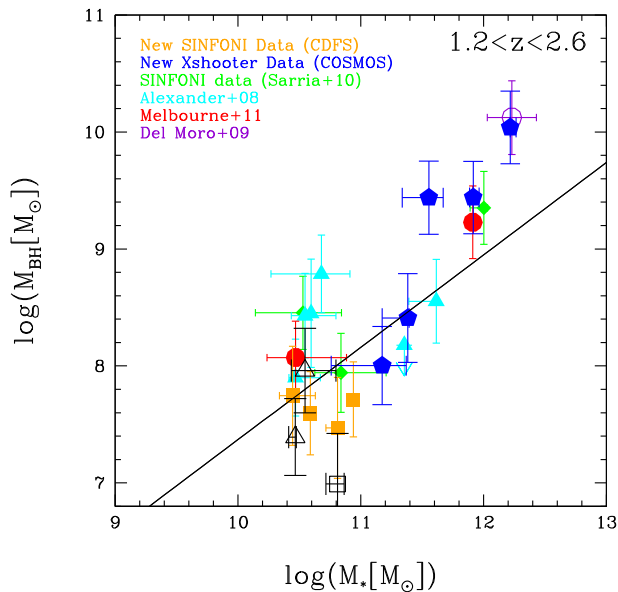
Figure 4. Scaling relation between M_{BH} and M_* for obscured AGN at $z \sim 1.2$–2.6 colour-coded as explained in the inset of the plot. The solid line is the local relation from Sani et al. (2011). For the three objects (CDFSX633, A1236+6214 and A1237+6203) for which the X-ray luminosity does not agree with the whole SED shape, we show two BH masses: colour-coded symbols correspond to the correct SED-based L_X while the open symbols (same symbols as the original ones) are the BH masses computed assuming the (lower) L_X as measured from X-ray data.

In this plot, we also include the comparison sample of optically type-1, blue QSOs at $1.2 < z < 2.1$ from Merloni et al. (2010) for which we re-computed the BH masses using equation (4) of Section 3, consistently with the dust-obscured, red ones.

We see that both blue and red QSOs show M_{BH}/M_* ratios increasing going to earlier epochs with red QSOs having slightly lower values at $z < 1.9$. This is evident in the upper panel of Fig. 5 where mean values and errors are shown for both populations. Since the M_* of A1637+4053 is poorly constrained by the SED fit and its M_{BH} is an upper limit due to its L_X, for the last bin of the red QSOs sample, we show both the mean value taking it into account (open circle) and excluding it (filled circle). The solid and dashed lines correspond to the redshift evolution derived for blue QSOs at $z < 2.1$ and extrapolated at higher redshift (Merloni et al. 2010). High-redshift red QSOs do not seem to follow such trend having on average lower values that remain constant at $z > 1.9$. The two distributions in the common redshift range ($1.2 < z < 2.1$) are shown in the right-hand panel of Fig. 5. According to a Kolmogorov–Smirnov statistics, the probability that the two samples are drawn from the same parent population is 10 per cent.

6.2 Possible biases

As discussed by e.g. Lauer et al. (2007) and Schulze & Wisotzki (2011), AGN flux limited samples are generally biased towards higher values of M_{BH}/M_*. The magnitude of this bias depends on the flux limit of the sample, i.e. it increases for brighter limiting fluxes, the underlying distribution functions and the intrinsic scatter in the $M_{BH}-M_*$ relation. Since both the unobscured AGN sample from Merloni et al. (2010) and the new sample of obscured AGN presented here are flux limited, i.e. X-ray flux limited from *XMM*-COSMOS and CDFS, both samples are affected by this selection bias. However, since the *Chandra* deep fields observations

are very deep, the expected bias is negligible, contrary to the *XMM*-COSMOS AGN samples for which a non-negligible bias is expected (as already discussed in Schulze & Wisotzki 2011). We quantified the magnitude of the bias using the framework presented in Schulze & Wisotzki (2011). We used their equation 29, assuming the $z=1$ BH mass function (BHMF) and Eddington ratio distribution function derived from the VVDS survey (Schulze et al. in preparation) and applying the limiting fluxes corresponding to the considered fields. The result is shown in Fig. 6. In this figure, we show with grey points the averages and their errors of the offsets from the local relation of the unobscured type-1 AGN sample and with orange squares and the blue pentagon the averages for CDFS-only and COSMOS-only obscured sources in the analysed sample, respectively.

The predicted bias in the case of no evolution is shown with a long-dashed grey line for the *XMM*-COSMOS flux limit. This has to be compared to the grey symbols. For the XShooter and SINFONI samples we consider as flux limits $f_X > 1 \times 10^{-14}$ erg cm^{-2} s^{-1} and $f_X > 1 \times 10^{-15}$ erg cm^{-2} s^{-1}, respectively, since above this fluxes the detection rate of broad Hα is >80 per cent and in this respect the incompleteness of the sample is negligible (see Section 2.1). The predicted biases in the case of no evolution for such limits are shown as a dot–dashed blue line in the first case and a dashed orange line for the latter case. The dot–dashed blue line has to be compared to the blue point while the dashed orange line to the orange squares. A slightly different treatment is needed for SMGs and ULIRGs which are primarily selected based on galaxy flux. For both samples, the additional AGN selection criterion, based on the Hα flux, leads to a positive bias of the order of $\sim$0.1 dex. As visible in the plot, the general trend for the sources of our sample as well as for the optical type-1 AGN from Merloni are reproduced by the bias predictions and would lead to the conclusion that both obscured and unobscured AGN lie on the local scaling relation up to $z \sim 2.6$. However, the observed samples show a higher mean value of $\Gamma(z)$ (in the case of COSMOS) due to observational biases, as described in Schulze & Wisotzki (2011).

Interestingly, the CDFS-only mean value at $z \sim 1.5$ is much lower than the predicted one, given the observational bias. In fact, it is important to keep in mind that the estimates of bias effects can suffer from some limitations and uncertainties: (i) an accurate prediction of the sample bias at a given redshift requires the knowledge of the underlying distribution functions, i.e. the spheroid mass function, the active BHMF and the Eddington ratio distribution function at that given redshift. Unfortunately, these distributions are still very poorly constrained at high-z, i.e. the spheroid mass function itself is basically unknown at high-z. Also the BHMF is best established at the high-mass end while the low-mass end is less well determined and the systematics not fully understood. Moreover, (ii) even considering all these uncertainties, a reliable bias prediction requires a sample with a well-defined selection function. This is the case for the optical type-1, blue AGN sample from Merloni which are selected from the whole *XMM*-COSMOS sample to be at $1.0 < z < 2.1$ and with broad lines in the spectra. The same is not true for our sources, made of different subsamples of objects for which spectroscopic NIR follow-up was performed.

7 EVOLUTION OF THE SCALING RELATION: COMPARISON WITH THE MODEL PREDICTIONS

In this section, we compare our observational results with the semi-analytic model from Menci et al. (2008, and reference therein) which allows us to follow the accretion on to SMBHs and the related AGN
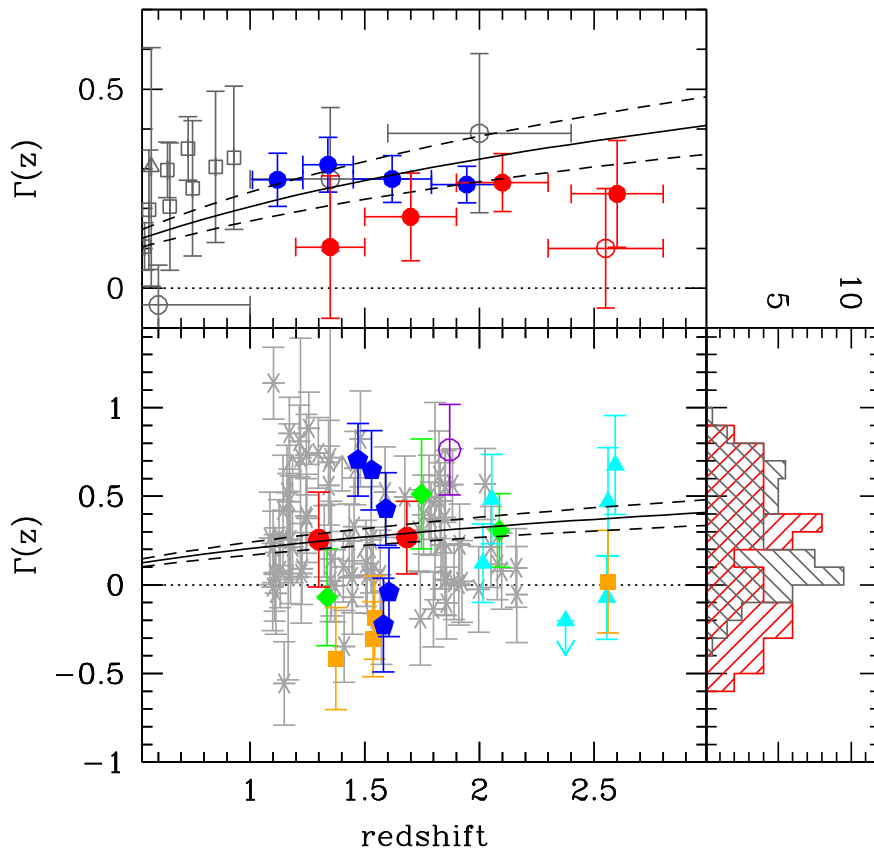
Figure 5. Main panel: redshift evolution of the offset measured for our sample from the local $M_{BH}-M_*$ relation. The offset $\Gamma(z)$ is calculated as the distance of each point to the Sani et al. (2011) correlation. Different colours and symbols correspond to the different subsamples (as in Fig. 4) while light grey symbols show the comparison sample of type-1, blue QSOs from Merloni et al. (2010). Solid dark grey line shows the best fit obtained by Merloni et al. (2010) rescaled using an average value to take into account the different formulas used in the BH masses computation. Upper panel: red symbols are the average values and errors of our data binned in four redshift bins compared to the blue QSOs from Merloni et al. (2010, blue symbols). Grey open symbols are objects from the literature: triangles are from Salviander et al. (2007, low-z) and Shields et al. (2003, high-z); squares from Woo et al. (2008) and circles from Peng et al. (2006). Right-hand panel: histogram of the blue (grey histogram) and red (red shaded histogram) QSOs populations in the common redshift range ($1.2 < z < 2.0$). For ease of comparison, the red histogram here has been multiplied by 4.

activity together with the evolution of galaxies. According to this model, galaxy interactions (i.e. both major and minor merging and fly-by events) trigger both starburst events and SMBH growth by inflow of cold gas in the galaxy disc which is destabilized and thus loses angular momentum. In addition, a second component of quiescent SF, corresponding to the gradual conversion of gas into stars on a longer time-scale (1 Gyr compared to $\sim 10^7$ yr of the starburst events), is always ongoing and responsible for the galaxy growth. The amount of gas available in the system, together with the galaxy interaction rate and their effectiveness in destabilizing the gas, are hence the driving parameters regulating both galaxy and SMBH growths. This model correctly describe the tight correlation between the BH mass and the stellar mass in the local Universe (Lamastra et al. 2010) and the evolution of the luminous AGN population over a wide range of redshift (see Menci et al. 2003, 2008). Such observables are also reproduced by several other semi-analytic models based on the assumption of interaction-triggered AGN implemented with accretion of hot gas and/or of instabilities in self-gravitating discs as additional triggers (see Bower et al. 2006; Croton et al. 2006; Hopkins et al. 2008; Marulli et al. 2008; Somerville et al. 2008; Guo et al. 2011; Fanidakis et al. 2012; Hirschmann et al. 2012). We compare our observations with the Menci model since it is ideally suited to our purpose. It is indeed

the only one that includes a physical description of AGN feedback providing a distribution of the AGN absorbing column density as a function of the luminosity and redshift tested against observations (see Menci et al. 2008).

By following the merging history of the galaxies at different epochs, it is possible to study the relative growth of BHs and host galaxies and to make predictions on the $M_{BH}-M_*$ relations at different epochs and as a function of various galaxy properties, e.g. mass, gas fraction and SFR.

Lamastra et al. (2010) showed that a typical prediction of such interaction-driven model is that the evolution of the $M_{BH}-M_*$ relation is stronger for increasing stellar or BH mass. Moreover, in agreement with the observations (e.g. Peng et al. 2006; Maiolino et al. 2007b; Merloni et al. 2010), they find that blue QSOs have a higher M_{BH}/M_* ratio at earlier epochs which decreases going to lower redshift and approaches the local relation. This trend is due to the fact that, in the early phases, the assembly of BH masses is extremely rapid and much faster than the stellar mass growth since these objects are hosted in the most massive haloes formed in dense environments in which both the interaction rate and the fraction of destabilized gas are large. On the contrary, going towards lower redshift, the decline of the interaction rate and of the destabilized gas fraction, suppresses the growth of BHs which is only due to
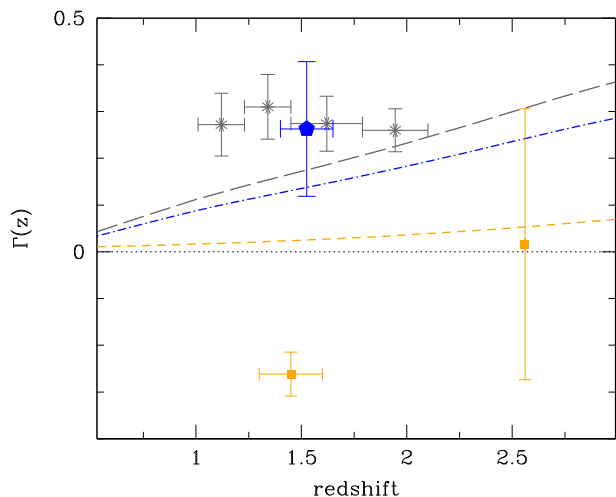
Figure 6. Grey circles are optically type-1 blue QSOs as in the upper panel in Fig. 5 while the average values with their errors for the CDFS-only and the COSMOS-only sources in our sample are shown as orange squares and the blue pentagon, respectively. Note that the orange square at $z \sim 2.5$ is made of only one object. The lines correspond to the expected luminosity bias computed considering the X-ray limiting fluxes of the X-Shooter sample (1×10^{-14} erg cm^{-2} s^{-1}; blue dot–dashed line), the SINFONI sample (1×10^{-15} erg cm^{-2} s^{-1}; orange dashed lines) and the *XMM*-COSMOS sample of optically blue QSOs (long-dashed grey line).

Figure 7. Contour plot of the predicted redshift evolution of the offset from the local relation $\Gamma(z)$ of $N_H > 10^{22}$ cm^{-2} and $R - K > 4$ AGN (Menci et al. 2008, and reference therein; see also Lamastra et al. 2010). The three filled contours correspond to different values of the fraction of objects with a given value of $\Gamma(z)$ at the considered redshift: 0.02, 0.1 and 0.2 from the lightest region to the darkest. The coloured dots with error bars denote our selected sample with the same coding as in Fig. 4.

galaxy interactions while quiescent SF still proceeds continuing to build up stellar mass.

In this section, we take a step forward and we follow in the Monte Carlo simulations only the X-ray-obscured, reddened QSO. The model includes a detailed treatment of AGN feedback which is directly related to the impulsive, luminous AGN phase (Menci et al. 2006, 2008) and is based on expanding blast waves as a mechanism to propagate outwards the AGN energy injected into the interstellar medium at the centre of galaxies. In the simulation, AGN are classified as obscured ($N_H \geq 10^{22}$ cm^{-2}) and unobscured ($N_H < 10^{22}$ cm^{-2}) on the basis of the neutral hydrogen column densities corresponding to the unshocked gas in the galaxy disc (equation 6 in Menci et al. 2008).

Since our sample is not a complete sample of sources with a clean selection but rather a collection of sources selected with slightly different criteria, it is not easy to compare them with the model predictions. X-ray obscuration and dust-reddening are common properties of all sources. For this reason, to select in the simulation the sample which is most similar to the data presented in this work, we performed a colour cut selecting only X-ray-obscured sources with red colours (i.e. $R - K > 4$ in Vega magnitudes). The simulated galaxy magnitudes are computed from the predicted SF and chemical enrichment histories using the single stellar population model of Bruzual & Charlot (2003) and the Salpeter IMF. The dust extinction affecting the above magnitudes is computed from the dust optical depth and applying the appropriate attenuation to the luminosity at various wavelengths. The comparison is shown in Fig. 7 where, together with the observational points (symbols and colour-code are as in Fig. 4), we plot the contour plot of the predicted redshift evolution of the offset from the local $M_{BH}-M_*$ relation ($\Gamma(z)$) for AGN with $\log(L_X) > 43.7$, $N_H > 10^{22}$ cm^{-2} and $R - K > 4$. These cuts are chosen to best reproduce the selection criteria of the observed sample. The three contour levels correspond to different values of
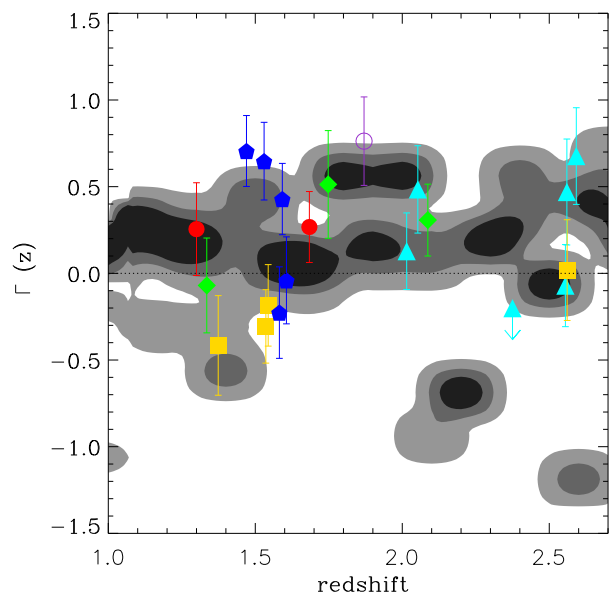
the fraction of objects with a given value of $\Gamma(z)$ at the considered redshift: 0.02, 0.1 and 0.2 from the lightest region to the darkest.

The model predicts that the $\Gamma(z)$ value for obscured and red QSOs slightly increases towards higher M_{BH}/M_*, with a lower offset than the one predicted for blue QSOs (see Lamastra et al. 2010). This is in excellent agreement with our observations. We do actually find that most of the sources in our sample lie well inside the contours of the model prediction and that red X-ray-obscured AGN and optical type-1, blue AGN follow a very similar path in the $M_{BH}-M_*$ plane.

8 DISCUSSION AND CONCLUSIONS

In this work, we have analysed a sample of X-ray-obscured, intermediate type, dust-reddened QSOs at $1.5 < z < 2.6$. Red, obscured QSOs are different from optical type-1 blue QSOs studied so far both in their host and nuclear properties, in that they are dusty and thus red and their nuclei are obscured. These objects may represent a 'transitional' phase in the AGN–galaxy co-evolving scenario as expected by the popular theoretical models by e.g. Hopkins et al. (2008) and Menci (2004). According to these models, in fact, major mergers are the main AGN fuelling mechanism and galaxy mergers are able to funnel a large amount of gas on to the nuclear regions in a short time-scale. In this phase, the AGN is indeed expected to be obscured and red. Moreover, the resulting high gas density in the central region of the galaxy triggers starburst events: red and obscured QSOs are expected to live in star-forming galaxies as found for most of our sources (90 per cent are main-sequence or starburst galaxies). Later, as radiative pressure on the dust grains begins to clear the dust and gas away during the blow-out phase in which evidence of outflows are expected, the AGN is revealed as an UV-luminous optical type-1, blue QSOs.

We have analysed the position of these sources in the $M_{BH}-M_*$ plane. We found a trend with the BH mass, i.e. while less massive red QSOs are about equally scattered below and above the local relation, the most massive ones are mainly located above it. The same trend with BH mass is predicted by the interaction-driven models since high-mass BHs form in the most biased regions of the primordial density field where high-redshift interactions were favoured (see e.g. Lamastra et al. 2010).

Looking at the average M_{BH}/M_* ratios as a function of redshift, we find that, similarly to unobscured, optically blue QSOs (e.g. Merloni et al., 2010), obscured red QSOs show a higher ratio compared to the local one, and the increase is higher going to higher redshift ($z \sim 2.6$).

Possible observational biases have been analysed. In particular, as discussed by e.g. Lauer et al. (2007) and Schulze & Wisotzki (2011), AGN flux limited samples are generally biased towards higher values of M_{BH}/M_*. Looking at the *XMM*-COSMOS samples and the CDFS sample, we find that the observed general trend in the $\Gamma(z)-z$ plane is very similar to the one predicted by the bias, thus suggesting that both obscured and unobscured AGN lie on the local scaling relation up to high-z but are observed at higher values of $\Gamma(z)$ due to observational biases.

However, we must keep in mind that the estimates of bias effects suffer from some limitations, i.e. they require the knowledge of the underlying distribution functions (the spheroid mass function, the active BHMF and the Eddington ratio distribution function) at the given redshift, and unfortunately, these distributions are still very poorly constrained at high-z.

The computed M_{BH}/M_* average values are consistent with or slightly lower (up to $z < 1.9$) compared to what has been found for blue QSOs (Merloni et al. 2010). This result suggests that in the analysed population of obscured, red QSOs the BH and their host stellar masses are already fully formed and thus their ratio is similar to what observed in optically blue QSOs.

Recently, Urrutia et al. (2012) studying a sample of 13 $z < 1$ luminous, dust-reddened QSOs found that these sources are preferentially located below the local scaling relation. This result has been interpreted as the evidence that these sources are in the intermediate phase (blow-out phase, see e.g. Hopkins et al. 2008) between the major-merger-induced starbursts which appear as ULIRGs and SMGs and the optical type-1, blue QSOs where we expect a rapid BH growth. In our sample, on the contrary, the BH has already grown up and the objects are located on average above the local relation, especially at the high-mass end. However, strong outflows are still visible, i.e. for the sources for which we have high-resolution spectra with good S/N of the [O III] region from X-Shooter, we indeed find compelling evidence of the presence of outflowing material in the ionized gas component (Brusa et al., 2014). This suggests that we are observing the final stage of such intermediate phase, when the BH growth is at its end but the AGN feedback has still not finished cleaning up the dust and nuclear gas. This is not so surprising considering that these sources do show broad lines in their optical lines (redshifted in the NIR): at least part of the obscuring material has already cleared-up and the AGN BLR are visible.

Larger samples expanding also to higher redshift are necessary in order to consolidate such results. Large area X-ray surveys with associated multiwavelength follow-up, such as XXL (Pierre 2012) and Stripe-82 (LaMassa et al. 2013) can be exploited to this end. Moreover, Integral Field Unit (IFU) spectroscopy and submm observations are fundamental to study in detail such rare objects and to provide a direct observational proof of quasar feedback through the detection of possible galactic-scale outflow and on its effect on the host galaxy SF by mapping the spatial distribution of the SFR (see e.g. Cano-Díaz et al. 2012).

REFERENCES

Alexander D. M. et al., 2003, AJ, 126, 539
Alexander D. M. et al., 2008, AJ, 135, 1968
Banerji M., McMahon R. G., Hewett P. C., Alaghband-Zadeh S., Gonzalez-Solares E., Venemans B. P., Hawthorn M. J., 2012, MNRAS, 427, 2275
Bennert V. N., Auger M. W., Treu T., Woo J.-H., Malkan M. A., 2011, ApJ, 742, 107
Bentz M. C., Peterson B. M., Netzer H., Pogge R. W., Vestergaaaard M., 2009, ApJ, 697, 160
Bongiorno A. et al., 2012, MNRAS, 427, 3103
Bower R. G., Benson A. J., Malbon R., Helly J. C., Frenk C. S., Baugh C. M., Cole S., Lacey C. G., 2006, MNRAS, 370, 645
Brusa M. et al., 2007, ApJS, 172, 353
Brusa M. et al., 2010, ApJ, 716, 348
Brusa M. et al., 2014, MNRAS, submitted
Bruzual G., Charlot S., 2003, MNRAS, 344, 1000
Calzetti D., Armus L., Bohlin R. C., Kinney A. L., Koornneef J., Storchi-Bergmann T., 2000, ApJ, 533, 682
Cano-Díaz M., Maiolino R., Marconi A., Netzer H., Shemmer O., Cresci G., 2012, A&A, 537, L8
Cappelluti N. et al., 2009, A&A, 497, 635
Chabrier G., 2003, PASP, 115, 763
Chapman S. C., Blain A. W., Smail I., Ivison R. J., 2005, ApJ, 622, 772
Cisternas M. et al., 2011, ApJ, 741, L11
Croton D. J. et al., 2006, MNRAS, 365, 11
Dale D. A., Helou G., 2002, ApJ, 576, 159
Decarli R., Falomo R., Treves A., Labita M., Kotilainen J. K., Scarpa R., 2010, MNRAS, 402, 2453
Del Moro A. et al., 2009, A&A, 493, 445
Dey A. et al., 2008, ApJ, 677, 943
Di Matteo T., Springel V., Hernquist L., 2005, Nature, 433, 604
Elbaz D. et al., 2011, A&A, 533, A119
Fanidakis N. et al., 2012, MNRAS, 419, 2797
Ferrarese L., Merritt D., 2000, ApJ, 539, L9
Feruglio C. et al., 2008, A&A, 488, 417
Fiore F. et al., 2003, A&A, 409, 79
Fiore F. et al., 2008, ApJ, 672, 94
Gandhi P., Horst H., Smette A., Hönig S., Comastri A., Gilli R., Vignali C., Duschl W., 2009, A&A, 502, 457
Giacconi R. et al., 2002, ApJS, 139, 369

Granato G. L., De Zotti G., Silva L., Bressan A., Danese L., 2004, ApJ, 600, 580

Greene J. E., Ho L. C., 2005, ApJ, 630, 122

Gültekin K., Cackett E. M., Miller J. M., Di Matteo T., Markoff S., Richstone D. O., 2009, ApJ, 706, 404

Guo Q. et al., 2011, MNRAS, 413, 101

Hainline L. J., Blain A. W., Smail I., Alexander D. M., Armus L., Chapman S. C., Ivison R. J., 2011, ApJ, 740, 96

Häring N., Rix H., 2004, ApJ, 604, L89

Hasinger G. et al., 2007, ApJS, 172, 29

Hirschmann M., Somerville R. S., Naab T., Burkert A., 2012, MNRAS, 426, 237

Hopkins P. F., Hernquist L., Cox T. J., Di Matteo T., Robertson B., Springel V., 2006, ApJS, 163, 1

Hopkins P. F., Hernquist L., Cox T. J., Kereš D., 2008, ApJS, 175, 356

Ilbert O. et al., 2010, ApJ, 709, 644

Jahnke K., Macciò A. V., 2011, ApJ, 734, 92

Jahnke K. et al., 2009, ApJ, 706, L215

Kaspi S., Smith P. S., Netzer H., Maoz D., Jannuzi B. T., Giveon U., 2000, ApJ, 533, 631

Kennicutt R. C., Jr, 1998, ARA&A, 36, 189

Kenter A. et al., 2005, ApJS, 161, 9

King A., 2005, ApJ, 635, L121

Kormendy J., Ho L. C., 2013, ARA&A, 51, 511

LaMassa S. M. et al., 2013, MNRAS, 436, 3581

Lamastra A., Menci N., Maiolino R., Fiore F., Merloni A., 2010, MNRAS, 405, 29

Lamastra A., Menci N., Fiore F., Santini P., 2013a, A&A, 552, A44

Lamastra A., Menci N., Fiore F., Santini P., Bongiorno A., Piconcelli E., 2013b, A&A, 559, A56

Lanzuisi G., Piconcelli E., Fiore F., Feruglio C., Vignali C., Salvato M., Gruppioni C., 2009, A&A, 498, 67

Lanzuisi G. et al., 2014, ApJ, 781, 105

Lauer T. R., Tremaine S., Richstone D., Faber S. M., 2007, ApJ, 670, 249

McGill K. L., Woo J.-H., Treu T., Malkan M. A., 2008, ApJ, 673, 703

McLure R. J., Dunlop J. S., 2001, MNRAS, 327, 199

Magnelli B. et al., 2012, A&A, 539, A155

Magorrian J. et al., 1998, AJ, 115, 2285

Mainieri V. et al., 2007, ApJS, 172, 368

Mainieri V. et al., 2011, A&A, 535, A80

Maiolino R. et al., 2006, A&A, 445, 457

Maiolino R., Shemmer O., Imanishi M., Netzer H., Oliva E., Lutz D., Sturm E., 2007a, A&A, 468, 979

Maiolino R. et al., 2007b, A&A, 472, L33

Manners J. C. et al., 2003, MNRAS, 343, 293

Marconi A., Hunt L. K., 2003, ApJ, 589, L21

Marconi A., Risaliti G., Gilli R., Hunt L. K., Maiolino R., Salvati M., 2004, MNRAS, 351, 169

Marulli F., Bonoli S., Branchini E., Moscardini L., Springel V., 2008, MNRAS, 385, 1846

Melbourne J. et al., 2011, AJ, 141, 141

Menci N., 2004, Ap&SS, 294, 15

Menci N., Cavaliere A., Fontana A., Giallongo E., Poli F., Vittorini V., 2003, ApJ, 587, L63

Menci N., Fontana A., Giallongo E., Grazian A., Salimbeni S., 2006, ApJ, 647, 753

Menci N., Fiore F., Puccetti S., Cavaliere A., 2008, ApJ, 686, 219

Merloni A. et al., 2010, ApJ, 708, 137

Merloni A. et al., 2014, MNRAS, 437, 3550

Mignoli M. et al., 2004, A&A, 418, 827

Mullaney J. R. et al., 2012, MNRAS, 419, 95

Mushotzky R. F., Cowie L. L., Barger A. J., Arnaud K. A., 2000, Nature, 404, 459

Onken C. A., Ferrarese L., Merritt D., Peterson B. M., Pogge R. W., Vestergaard M., Wandel A., 2004, ApJ, 615, 645

Osterbrock D. E., 1981, ApJ, 249, 462

Papovich C. et al., 2006, ApJ, 640, 92

Park D., Kelly B. C., Woo J.-H., Treu T., 2012, ApJS, 203, 6

Peng C. Y., 2007, ApJ, 671, 1098

Peng C. Y., Impey C. D., Ho L. C., Barton E. J., Rix H., 2006, ApJ, 640, 114

Peterson B. M., 2013, Space Sci. Rev., 60P, available online at: http://link.springer.com/article/10.1007%2Fs11214-013-9987-4

Peterson B. M. et al., 2004, ApJ, 613, 682

Piconcelli E., Guainazzi M., Cappi M., Jimenez-Bailon E., Schartel N., 2005, A&A, 432, 835

Pierre M., 2012, in Science from the Next Generation Imaging and Spectroscopic Surveys, available online at: http://www.eso.org/sci/meetings/2012/surveys2012/program.html, id.45

Prevot M. L., Lequeux J., Prevot L., Maurice E., Rocca-Volmerange B., 1984, A&A, 132, 389

Richards G. T. et al., 2006, ApJS, 166, 470

Rodighiero G. et al., 2011, ApJ, 739, L40

Salviander S., Shields G. A., 2013, ApJ, 764, 80

Salviander S., Shields G. A., Gebhardt K., Bonning E. W., 2007, ApJ, 662, 131

Sani E., Marconi A., Hunt L. K., Risaliti G., 2011, MNRAS, 413, 1479

Sargent M. T., Béthermin M., Daddi E., Elbaz D., 2012, ApJ, 747, L31

Sarria J. E., Maiolino R., La Franca F., Pozzi F., Fiore F., Marconi A., Vignali C., Comastri A., 2010, A&A, 522, L3

Schawinski K., Dowlin N., Thomas D., Urry C. M., Edmondson E., 2010, ApJ, 714, L108

Schramm M., Silverman J. D., 2013, ApJ, 767, 13

Schulze A., Wisotzki L., 2011, A&A, 535, A87

Shen Y., 2013, Bull. Astron. Soc. India, 41, 61

Shields G. A., Gebhardt K., Salviander S., Wills B. J., Xie B., Brotherton M. S., Yuan J., Dietrich M., 2003, ApJ, 583, 124

Silk J., Rees M. J., 1998, A&A, 331, L1

Somerville R. S., Hopkins P. F., Cox T. J., Robertson B. E., Hernquist L., 2008, MNRAS, 391, 481

Szokoly G. P. et al., 2004, ApJS, 155, 271

Urrutia T., Lacy M., Becker R. H., 2008, ApJ, 674, 80

Urrutia T., Lacy M., Spoon H., Glikman E., Petric A., Schulz B., 2012, ApJ, 757, 125

Vernet J. et al., 2011, A&A, 536, A105

Vestergaard M., Peterson B. M., 2006, ApJ, 641, 689

Wang J.-G. et al., 2009, ApJ, 707, 1334

Whitaker K. E., van Dokkum P. G., Brammer G., Franx M., 2012, ApJ, 754, L29

Woo J., Treu T., Malkan M. A., Blandford R. D., 2008, ApJ, 681, 925

Young M. et al., 2012, ApJ, 748, 124

This paper has been typeset from a TEX/LATEX file prepared by the author.